communications physics

ARTICLE

https://doi.org/10.1038/s42005-023-01208-x OPEN

Impact of noise on spinodal dewetting of liquid-liquid films

Roghayeh Shiri[1,3], Leonie Schmeller[2,3], Dirk Peschka[2✉], Ralf Seemann[1✉] & Barbara Wagner[2]

Spinodal dewetting provides fundamental insights into the physics at interfaces, such as van der Waals forces driving dewetting, dissipation processes or thermal fluctuations. The dewetting process of liquid bilayer systems still raises open problems involving two coupled moving interfaces. Comparison of experimental results of spinodally dewetting liquid polystyrene films from liquid polymethylmethacrylate substrates, with predictions from linear stability analysis, we demonstrate that both the spinodal wavelength and the rupture times show significant differences. Key for this discrepancy is the altered mode selection process due to the initial surface roughness of the liquid-air and liquid-liquid interfaces, which is perturbed by partially correlated colored noise in the linearly unstable region. The strong effect of noise on mode selection and rupture time is confirmed by comparing experimental results with numerical solutions of the full dynamic nonlinear model and suggest new strategies to include thermal fluctuations into modeling these processes.

[1] Department of Experimental Physics & Center for Biophysics, Universität des Saarlandes, Saarbrücken 66123, Germany. [2] Weierstrass Institute for Applied Analysis and Stochastics, Mohrenstrasse 39, Berlin 10117, Germany. [3] These authors contributed equally: Roghayeh Shiri, Leonie Schmeller. ✉email: dirk.peschka@wias-berlin.de; r.seemann@physik.uni-saarland.de

Dewetting flows with moving interfaces and moving contact lines on solid substrates[1–3] and on liquid substrates[4,5] have been studied extensively for many decades. This lead to a range of different theoretical approaches, that include, apart from hydrodynamic theory and phase-field models, also concepts of van der Waals interface potentials and wall slip, and continues to provide many fundamental insights to the moving contact-line problem and pattern formation in free surface flows[6–15]. In many ways, the dewetting of a viscous liquid from another immiscible viscous substrate is similar to that on a solid substrate: When a uniform liquid layer is energetically unfavorable, then it destabilizes either spinodally or by heterogeneous nucleation[16–23]. In a small intermediate regime both systems allow for an instability that evolves through the creation of satellite holes[24]. Driven by surface energies, resulting holes grow over time and lead to characteristic dewetting rims that ultimately evolve into arrays of stationary droplets[25]. Spatio-temporal fluctuations have been found relevant to explain discrepancies of time scales for early stages of nonlinear spinodal nucleation for thin films on solid substrates[26–28].

Besides all similarities, dewetting from a liquid substrate is also strikingly different to that from a solid substrate and thus fundamentally interesting: Firstly, the existence of a liquid substrate naturally cures the contact line singularity and thereby provides an ideal modeling system to study interfacial and contact line dynamics – in that respect de Gennes called liquid substrates the "epitome of perfection"[29,p. 169]. Secondly, the interaction of the viscous flow through the liquid–liquid interface leads to a nontrivial coupling of dissipative processes in the flow and in the substrate that can potentially affect dewetting and pattern formation processes[30–36]. This coupling provides additional complexity and leads to alternative pathways in the early and late stages of the dewetting process.

The initial period of the polymer-polymer spinodal dewetting was already investigated experimentally, demonstrating the existence of capillary waves at the interface of polystyrene (PS) and polymethylmethacrylate (PMMA)[32,37–40], but not finding a similar quantitative agreement as was observed for polymers dewetting from solid substrates. Theoretical works used linear stability analysis[21,23] and numerical simulations[41–43] for the analysis of the spinodal instability. In these studies it was found that by changing the thickness ratio of the layers one can switch between different dominant unstable modes. Based on similar thin-film models, the impact of interfacial slip on the instability has been investigated in ref. [44], and further extensions to surfactant-driven flows and more complex energetic models with sharp-moving contact lines were developed in ref. [45–47]. Instabilities of thick films with electric fields were studied in ref. [48] and quantitative agreement with linear stability analysis was found. However, a quantitative comparison of numerical modeling and theoretical predictions with experimental results for van der Waals-driven spinodal breakup and thus an in depth understanding of the microscopic processes driving liquid–liquid dewetting is still missing.

To elucidate this, we address the spinodal dewetting of a PS-PMMA bilayer system and investigate the onset of evolution through direct Atomic Force Microscopy (AFM) measurements and complementary spectral analysis. Direct comparison of experiments with classical linear theory and with numerical simulations of the full nonlinear dynamic model that take account of colored correlated noise at both liquid interfaces show a significant impact of noise on mode selection and rupture time. These results show the need of new theoretical approaches to study the spinodal dewetting of bilayers. In particular, for these time and length scales, one should augment the usual approach via continuum models to include thermal fluctuations of rough interfaces.

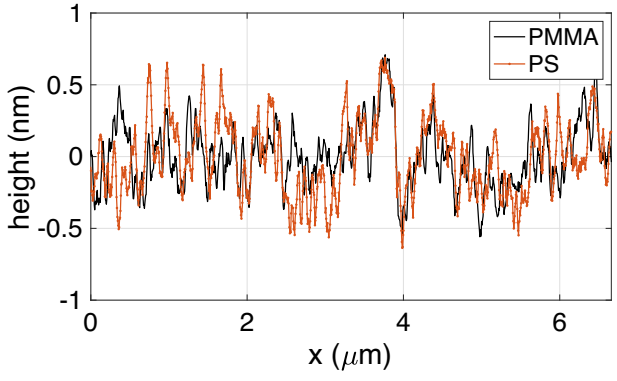

Fig. 1 Cross sections of initially prepared polystyrene (PS) and polymethylmethacrylate (PMMA) interfaces. The interfaces were both scanned by atomic force microscopy and aligned and reveal distinct positive correlation $\langle (h-\langle h\rangle)(h_{\mathrm{PMMA}}-\langle h_{\mathrm{PMMA}}\rangle)\rangle \approx +\frac{1}{2}$, dominated by modes on the micrometer scale. Establishing correlations on the spinodal length-scale is not possible by experimental precision.

Results and discussion

Experimental observation. We explore the spinodal dewetting of liquid polystyrene (PS) layers with initial thickness in the range $2\,\mathrm{nm} \le h^0_{\mathrm{PS}} \le 8.2\,\mathrm{nm}$ from a liquid polymethylmethacrylate (PMMA) layer with an initial thickness $h^0_{\mathrm{PMMA}} = 111\,\mathrm{nm}$ or 219 nm. The PMMA layer is supported from below by a solid silicon substrate and above the PS layer is an air phase. The chain lengths of PS and PMMA were selected so that the liquid polymers have approximately equal viscosities for the experimentally considered temperatures $120°\mathrm{C} \le T \le 130°\mathrm{C}$. The layered system is prepared from solution in the glassy state as described in the methods section.

The topographies of PS-air and PS-PMMA interface right after preparation can be seen as overlapped cross sections in Figs. 1 and 2a, f. The root mean square values of initial corrugations averaged over several samples are $R_q = (0.28 \pm 0.02)\,\mathrm{nm}$ for the buried PS-PMMA interface and $R_q = (0.30 \pm 0.04)\,\mathrm{nm}$ for the top PS-air interface. The most striking observation in the topography shown in Fig. 1 is that the (random) corrugations of the PS layer and the PMMA layer are in fact positively correlated on a typical length scale of a micrometer. Due to practical limitations matching the PS-air and the PS-PMMA interfaces and due to the dominance of large wavelengths in the spectral composition of this noise Fig. 3, no correlation can be established for corrugations on the length scales $\lesssim 250\,\mathrm{nm}$ that are relevant for the spinodal dewetting.

When heating the initially prepared PS-PMMA bilayer system to a temperature above the glass transition temperature where both polymers are liquid, the surface topography evolves over time, Fig. 2b–e, g-h. Due to the about twenty times larger surface tension of the PS-air interface compared to the PS-PMMA interface, there is no clearly visible topographic change of the PS-air interface until small downward indentations appear rather late at $t = 990\,\mathrm{s}$. This is in contrast to the PS-PMMA interface, whose amplitude is visibly growing already at early times. As soon as the PS-air and PS-PMMA interfaces meet, holes form and grow over time, which is then visible in both experimental interface topographies.

To quantify the evolution of the roughness and the onset of spinodal dewetting, power spectral densities (PSD), which are defined in Supplementary Note 6, are shown in Fig. 3a, b. The

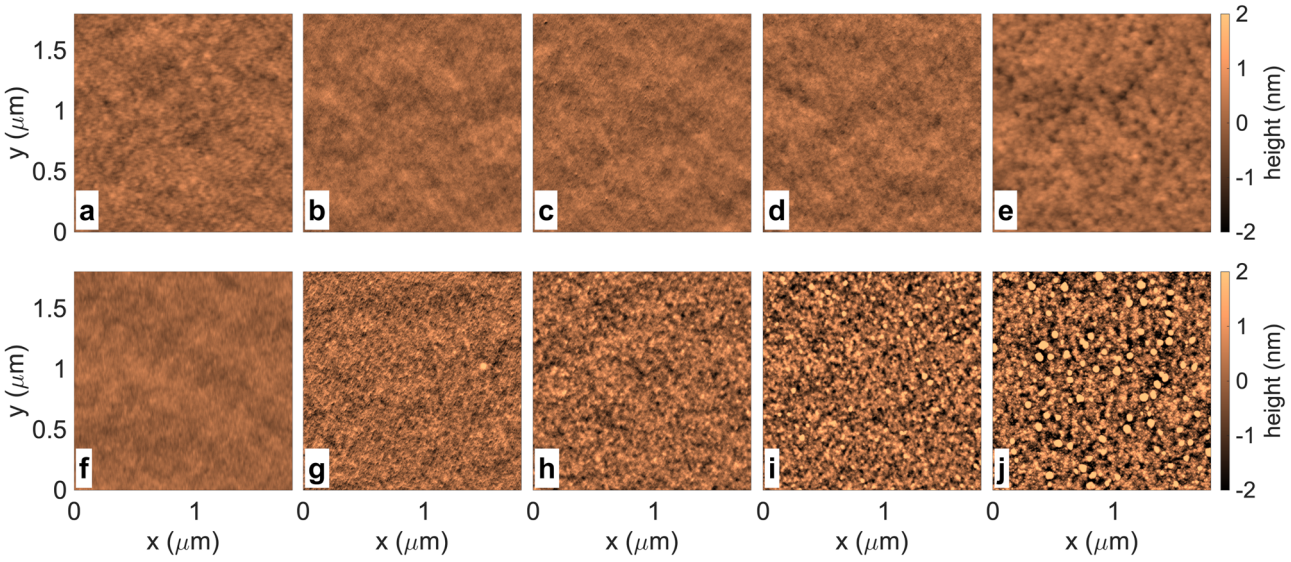

Fig. 2 Evolution of polystyrene (PS)-air and PS-polymethylmethacrylate (PMMA) interface. Topographies **a**–**e** of the PS-air interface, $h_{PS}(t, \boldsymbol{x}) - h^0_{PS}$ and **f**–**j** of the PS-PMMA interface, $h_{PMMA}(t, \boldsymbol{x}) - h^0_{PMMA}$ obtained by atomic force microscopy (AFM) at dewetting times of $t = 0$ s, 90 s, 240 s, 525 s, 990 s from left to right. Experiments were performed at $T = 124$ °C with $h^0_{PS} = 6$ nm and $h^0_{PMMA} = 111$ nm. Holes have formed at $t = 525$ s as clearly visible by upward deformations of the PS-PMMA interface (bright spots in panel **i**) and faintly visible in downward deformations of the PS-air interface (dark spots in panel **d**). To image the buried PS-PMMA layer by AFM, the PS film was removed by a selective solvent (see methods), accordingly, the shown time series is composed of five samples that were prepared with same film thicknesses and annealed for the given time. Times $t > 0$ denote the time how long the individual samples were placed on a hot plate; $t = 0$ refers to the situation before annealing.

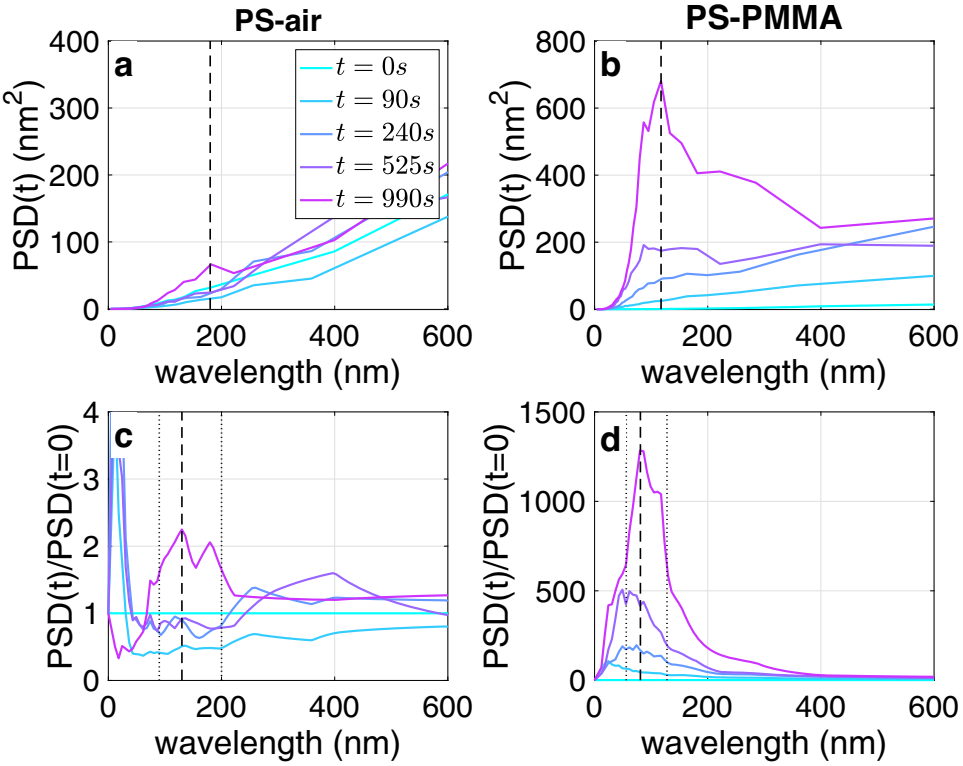

Fig. 3 Power spectral densities (PSD) of polystyrene (PS)-air and PS-polymethylmethacrylate (PMMA) interfaces. PSDs at different dewetting times for **a** PS-air and **b** of PS-PMMA interface are obtained from the data displayed in Fig. 2. The corresponding normalized PSD of PS-air and PS-PMMA interface are shown in **c**, **d**. Normalization at t is performed with respect to the initial density, i.e., $\mathrm{PSD}(t, k)/\mathrm{PSD}(0, k)$. The vertical dashed black lines show the local maxima and thin dotted black lines the corresponding errors obtained from full width at half maximum.

initial PSDs of the PS-air interface and of the PS-PMMA both reveal a dominance of large wavelength, i.e. the initial noise is colored. During dewetting, the PSD of the PS-air interface shows no clear evolution of surface waves and no clear wavelength. The PS-PMMA interface, on the other hand, shows a clear evolution of the PSD over time with a slow decay toward longer wavelengths. To display the changes in the PSD more clearly, we normalized the PSD at time t with respect to the initial PSD at

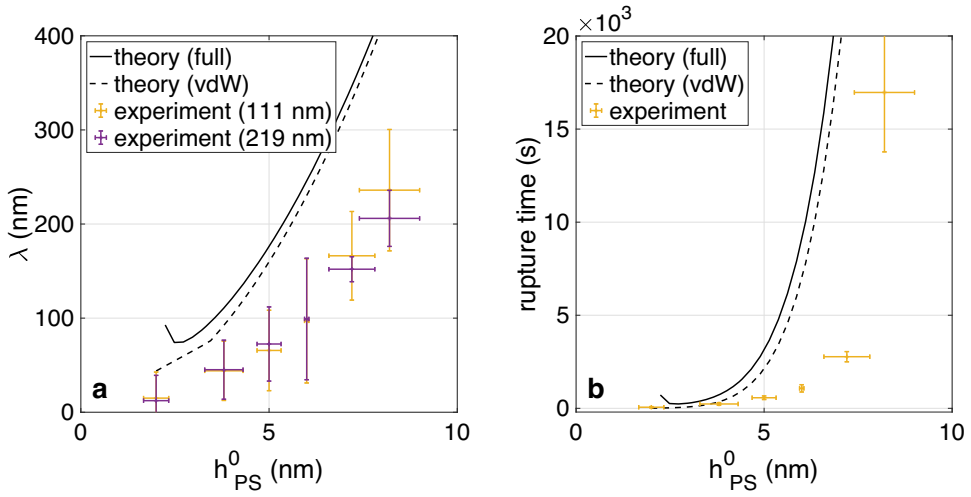

Fig. 4 Spinodal wavelength and rupture time depending on polystyrene (PS) film thickness. a Spinodal wavelength of PS films with thickness $2\,\mathrm{nm} \le h^0_{PS} \le 8.2\,\mathrm{nm}$ on polymethylmethacrylate (PMMA) with $h^0_{PMMA} = 111\,\mathrm{nm}$ (orange crosses) and $h^0_{PMMA} = 219\,\mathrm{nm}$ (purple crosses) determined from normalized power spectral densities (PSD). The black lines are predictions from linear stability analysis (1) using the full intermolecular potential (solid line) or using only the long-ranged van der Waals potential (dashed line). **b** Experimentally determined spinodal breakup time (orange crosses) compared to rupture time from linear stability analysis for PMMA thickness of $h^0_{PMMA} = 111\,\mathrm{nm}$. The experimental rupture times were re-scaled for a dewetting temperature of $T = 125\,°\mathrm{C}$ corresponding to a viscosity of $\mu_{PS} \approx 2.7$ MPas and $\mu_{PMMA} \approx 1.9$ MPas. Error bars denote statistical errors including the uncertainty of individual measurements. Theoretical values assume $\mu_{PMMA} = \mu_{PS} = 1.9$ MPas and an assumed overlap of $w^{\mu}_{PS} = 0.6\,\mathrm{nm}$. In Supplementary Note 3, this data is shown in a double-logarithmic plot to indicate possible power-law dependencies of wavelength and rupture time on h^0_{PS}.

time $t = 0$ as shown in Fig. 3c, d. Here, the existence of a fastest-growing wavelength is much more pronounced with $\lambda_{exp,PS\text{-}PMMA} = (90 \pm 50)\,\mathrm{nm}$ at $t = 990\,\mathrm{s}$ at the PS-PMMA interface, where the errors are due to the half width at half height of the maximum in the PSD. Similarly, from the normalized PSD of the PS-air interface we can obtain a slight reduction of the initial roughness for early times and a faintly visible fastest-growing mode $\lambda_{exp,PS\text{-}air} = (130 \pm 50)\,\mathrm{nm}$ at the time step after hole rupture $t = 990\,\mathrm{s}$. Note that the spinodal wavelength were determined at times, where corrugations are clearly detectable at both interfaces and thus can be correlated. The thus determined fastest-growing wavelengths also agree with the preferred distance of holes obtained from a pair correlation function, which is $\lambda_{exp,holes} = (86 \pm 16)\,\mathrm{nm}$ for this example (Supplementary Note 7).

In general, a preferred, respectively fastest-growing wavelength can be observed at the PS-PMMA interface already well before film rupture and at the PS-air interface just before rupture. Within the experimental precision, both wavelength taken at the moment of rupture agree with each other and also with the preferred distance of holes right after their formation. Therefore, we conclude that it is in fact a spinodal process that leads to the evolution of the topography and finally to film rupture.

Although the initial roughness of the PS-air and the PS-PMMA interfaces are positively correlated for wavelengths of $\sim 1\,\mu\mathrm{m}$, Fig. 1, at later times the corrugations of $\lesssim 250$ nm relevant for spinodal film rupture are growing downwards at the PS-air interface and upwards at the buried PS-PMMA interface and the surface evolution leading to spinodal rupture is therefore negatively correlated. The latter can also be seen when overlapping the material contrast (phase contrast) and the measured AFM surface topography of an evolving PS-air interface (Supplementary Note 8). The observed spinodal wavelength increases for increasing PS film thickness between $h^0_{PS} = 2\,\mathrm{nm}$ and $h^0_{PS} = 8.2\,\mathrm{nm}$ and is independent from the thickness of the liquid PMMA substrate, provided the PMMA layer is sufficiently thick, as confirmed experimentally for $h^0_{PMMA} = 111\,\mathrm{nm}$ and $h^0_{PMMA} = 219\,\mathrm{nm}$, Fig. 4a. The amplitude growth of the preferred spinodal wavelength also leads to a characteristic rupture time that also increases with PS film thickness h_{PS}, Fig. 4b.

To ensure that the dewetting dynamics are neither too fast (shorter than 5 min) nor too slow (longer than 1 d) and match the limited acquisition time of the AFM, we adjusted the temperature in the experiment in the range between 120°C and 130°C. However, for a uniform presentation, all resulting times in Fig. 4b are rescaled to a temperature of 125 °C, assuming a linear dependence between breakup time and polymer viscosity. The breakup times were taken as the heating time required to detect the first hole in an AFM scan. Therefore the breakup time might depend slightly on scan size. However, as the scan areas are large compared to the spinodal wavelength and the statistics of hole sites is reasonably large, this uncertainty is expected to be smaller than the typical acquisition time for each AFM scan of around 4 min.

Note that the experimentally accessible PS thickness range is limited. On the one hand, it is not possible to prepare arbitrarily thin PS films. On the other hand, it is not possible to reliably detect a spinodal wavelength for PS film thicknesses well above $h^0_{PS} \approx 8\,\mathrm{nm}$. The likely reason for that is that the driving van der Waals forces weaken for increasing film thickness leading to long spinodal rupture times and thus heterogeneous nucleation will eventually be faster. This reasoning is supported by previous studies on solid substrates with similar Hamaker constant, where spinodal dewetting was also observed only in a comparable layer thickness range[17–20,49,50].

Predictions of the linear theory. The wavelength and rupture time are determined by a linear stability analysis (see Methods) based on the long-wave approximation describing a PS layer $h_{PS}(t, \boldsymbol{x})$ dewetting from a PMMA layer $h_{PMMA}(t, \boldsymbol{x})$, driven by an intermolecular potential $\Phi(h)$. Perturbation about the initially unperturbed film of thickness $\boldsymbol{h}^0 = (h^0_{PMMA}, h^0_{PS})$ results in an eigenvalue problem that yields stable (index s) and unstable

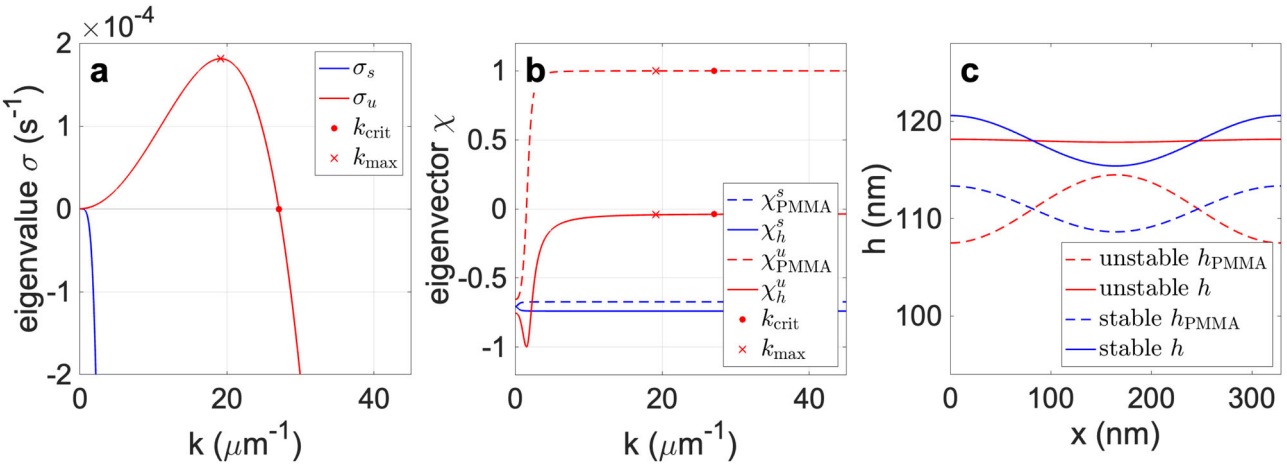

Fig. 5 Results from linear stability analysis. a Eigenvalues $\sigma_{s,u}(k)$ of stable and unstable branch with $1/\sigma_u = 9400$ s at $k_{\max}$. **b** Normalized (but not orthorgonal) eigenvectors $\boldsymbol{\chi}_{s,u}$ for the stable and unstable branch with $\chi_h = \chi_{\mathrm{PS}} + \chi_{\mathrm{PMMA}}$. **c** Initial perturbation $\boldsymbol{h} = \boldsymbol{h}^0 + \delta\boldsymbol{\chi}_\alpha \cos(k_x x)\cos(k_y y)$ using an unstable or stable eigenmode for $h^0_{\mathrm{PMMA}} = 111$ nm and $h^0_{\mathrm{PS}} = 7$ nm (amplitude exaggerated) for $k = k_{\max}$ using the physical parameters of the polystyrene (PS)-polymethylmethacrylate (PMMA) system. Stable deformations (blue) are positively correlated, whereas in the unstable case (red) the PS film is thinner where the PMMA film is thicker, i.e., negatively correlated.

(index u) k-dependent eigenvalues

$$\sigma_{s,u}(k) = -\frac{1}{2}k^2\mathrm{tr}\,(\boldsymbol{M}) \pm k^2\sqrt{\frac{1}{4}\mathrm{tr}\,(\boldsymbol{M})^2 - \det(\boldsymbol{M})}, \qquad (1)$$

where $\boldsymbol{M} \in \mathbb{R}^{2\times 2}$ denotes the matrix defined in the methods section. We observe that in general the initial evolution of the system will be dominated by dampening of stable modes for all k and the growth of unstable modes with $0 \le k = |\boldsymbol{k}| \le k_{\mathrm{crit}}$. Based on the linear theory, the spinodal rupture time t_{rup} for initial data $\boldsymbol{h}^0$ and k is

$$t_{\mathrm{rup}} = \frac{1}{\sigma_u(k)}\log\left(\frac{h^0_{\mathrm{PS}}}{w^u_{\mathrm{PS}}}\right), \qquad (2)$$

where the rupture time depends on the wavenumber k for $\sigma_u(k) > 0$. Here t_{rup} depends on the overlap with the initial perturbation $\boldsymbol{h}(t=0) = \boldsymbol{h}_0 + \delta\boldsymbol{h}e^{i\boldsymbol{k}\cdot\boldsymbol{x}}$ with the unstable mode, i.e., based on the unique decomposition $\delta\boldsymbol{h} = \delta_u\boldsymbol{\chi}_u + \delta_s\boldsymbol{\chi}_s$ with linear independent eigenvectors $\boldsymbol{\chi}_{s,u} = (\chi^{s,u}_{\mathrm{PMMA}}, \chi^{s,u}_{\mathrm{PS}})$ and we get $w^u_{\mathrm{PS}} = \delta_u\chi^u_{\mathrm{PS}}$.

Note that such a dependence of rupture times on the overlap is not present for single-layer thin films, since the linear stability only features a single unstable branch. Usually the fastest-growing mode $\sigma_{\max} = \sigma_u(k_{\max}) = \mathrm{argmax}_{\boldsymbol{k}}\sigma_u(\boldsymbol{k})$, determines the rupture time $t \sim (\sigma_{\max})^{-1}$, if $\boldsymbol{w}_u$ does not or only weakly depend on k (see Supplementary Note 3). The eigenvalues $\sigma_{s,u}$ together with the corresponding eigenvectors $\boldsymbol{\chi}_{s,u}$ and the interface deformations are plotted in Fig. 5 for $h^0_{\mathrm{PS}} = 7$ nm, where $1/\sigma_u(k_{\max}) = 9400$ s and $\lambda_{\max} = 2\pi/k_{\max} = 340$ nm. The components of the unstable eigenvector shown in Fig. 5b change from same sign for small wave vectors $0 < k < 3(\mu\mathrm{m})^{-1}$ to opposite sign for $3(\mu\mathrm{m})^{-1} \le k \le k_{\mathrm{crit}}$. This means that also positively correlated long surface waves are on the unstable branch but, due to $0 < \sigma_u(k) \ll \sigma_u(k_{\max})$, have a growth factor much slower than that for the spinodal wavelength. This is consistent with the experimentally observed positively correlated surface waves on the micrometer scale that persist or even slightly grow in amplitude until rupture time Figs. 1 and 3.

Comparison of experiments and linear stability. Qualitatively, the increase of the experimentally observed spinodal wavelength and of the rupture time with increasing PS film thickness h^0_{PS} agrees with predictions of the linear stability analysis, Fig. 4. Also, the negative correlation of PS-air and PS-PMMA interface at rupture and the weak dependence of the spinodal wavelength on the PMMA film thickness agrees with predictions from the linear stability analysis. However, linear theory systematically predicts both longer spinodal wavelengths and longer rupture times than observed experimentally. This discrepancy in the wavelengths is unexpected as the linear stability analysis has been very successful in predicting spinodal wavelength when a thin polymer film dewets from a solid support[17,19,20], which includes the computation of the Hamaker constant[51].

Discrepancies in theoretical rupture times based on linear stability and experiments were already reported and different explanations are discussed in literature, e.g. nonlinear acceleration and thermal fluctuations[21,23,27,28,41,52–55]. These effects can be significant and their combined impact on rupture times and wavelengths will be discussed in the following section. However, before coming back to fluctuations and nonlinearities we explain why the observed discrepancies are most likely not due to uncertainties in the physical parameters or caused by other effects.

The specific choice of the intermolecular potential has only a small effect on wavelength, e.g., for $h_{\mathrm{PS}} = 7$ nm the unstable wavelength $\lambda_{\max} = 340$ nm decreases at most by 5 % upon different choices for the short-range potential and the rupture time decreases not more than 25 %, which can also be seen in the comparison of wavelength and rupture time for full and only long-ranged potential plotted in Fig. 4. Also, any uncertainty of the Hamaker constant and thus in the driving forces will directly impact the predicted spinodal wavelength and breakup times. For example, a Hamaker constant more than twice as large as the calculated one, (5), would be needed to explain the quantitative difference in rupture time but would still not be sufficient to match the wavelength. However, such a large Hamaker constant is well beyond the variations expected from uncertainties of the dielectric properties that were used to calculate it. For the considered system, a dependence of the spinodal wavelength on the exact viscosity or viscosity ratio was not observed in the linear theory. For fixed viscosity ratio, any change of the viscosities directly translates into a change of the time scale, which might be the greatest source of uncertainty for the rupture time. At fixed PMMA viscosity μ_{PMMA}, having a viscosity ratio of $\mu = 1$ instead of $\mu = 1.4$ will cause a reduction in rupture time of < 5 %.

Similarly, working with a reduced PS viscosity $\mu = 0.1$ reduces the rupture time by less than a factor two (see Supplementary Note 11).

Stress relaxation times for PMMA are of the order $\tau \sim 10^0$ s and for PS of the order $\tau \sim 10^1$ s, e.g.[36,56]. However, since $\tau \ll t_{\mathrm{rup}} \sim 10^3$ s we expect no impact of visco-elastic effects on the rupture time, which justifies to consider both liquids as Newtonian. Other dissipative effects such as slip at the polymer-polymer interface can also decrease the rupture time. For the example of $h_{\mathrm{PS}} = 7$ nm and an interfacial slip-length of $b_i = 10$ nm, the inverse of the maximally unstable eigenvalue reduces from $1/\sigma_u = 9400$ s to $1/\sigma_u = 5800$ s and correspondingly reduces the rupture time t_{rup}; we refer to[44] for a detailed discussion on slip. But also this reduction in breakup time due to slip is way to small to explain the observed deviations. However, larger slip lengths can be excluded based on previous quantitative comparison of experimentally and theoretically determined rim profiles and dewetting rates for the same polymer system[36]. Also, the interfacial width $w = a/\sqrt{2\chi}$ between the immiscible polymers PS and PMMA might contribute to the difference of predicted and observed wavelength of the spinodal instability but has not been discussed in literature so far. Here, χ is the Flory-Huggins interaction parameter and a the segment length. Commonly reported values for PS/PMMA interfaces lie in the range $w = 2\ldots5$ nm[57,58] with dependence on film thickness[37] and molecular weight[59], which might affect the molecular roughness of the PS-PMMA interfaces.

Only when combining all the above mentioned quantitative effects while assuming that all possible uncertainties act in the same direction, the discrepancy between experimental results and predictions from linear stability analysis could be drastically diminished. However, this seems rather unlikely. In the following section, we therefore investigate the influence of initial surface roughness and nonlinear effects, which seem more likely to explain the observed differences between experimental results and theoretical predictions.

Nonlinear evolution of spinodal dewetting. An in-depth discussion of the initial surface roughness is essential for this bilayer system, as the existence of two solution branches caused by the existence of two mobile interfaces is a profound difference to the dewetting from a solid substrate. Here, the discussion of the overlap of the initial perturbation with the stable and unstable branch of the dispersion relation, Fig. 5, is particularly important.

The existence of an correlated initial surface roughness of the PS-air and the PS-PMMA interfaces is apparent from the topographic data shown in Fig. 1. Together with a more detailed analysis in the Supplementary Note 5, we investigate the combined impact of nonlinearities and noisy initial data. Specifically, we investigate the impact of different correlated initial PS-air and PS-PMMA interfaces in the nonlinear evolution problem (3) on the rupture time and on the unstable wavelength using numerical simulations. For that we choose

$$h(t=0,\boldsymbol{x}) = h^0 + \delta h\, \xi(\boldsymbol{x}),$$
$$h_{\mathrm{PMMA}}(t=0,\boldsymbol{x}) = h^0_{\mathrm{PMMA}} + \delta h_{\mathrm{PMMA}}\, \xi_{\mathrm{PMMA}}(\boldsymbol{x}),$$

for the total film thickness defined as $h = h_{\mathrm{PS}} + h_{\mathrm{PMMA}}$. Guided by the experiments, we restrict our considerations to small perturbations δh_α of a uniform thickness h^0_α, which might be suited to explain the discrepancy between experimental measurements and linear stability. To represent the initial roughness of a PS layer with $h^0_{\mathrm{PS}} = 7$ nm and a PMMA layer with $h^0_{\mathrm{PMMA}} = 111$ nm, we use independent normally distributed data $\xi_\alpha(\boldsymbol{x})$, where the initial layer thicknesses are perturbed with white (Gaussian) noise with $\delta h = \delta h_{\mathrm{PMMA}} = 0.7$ nm. As a result, the observed rupture times $t_{\mathrm{sim}} = 22 \times 10^3$s defined by appearance of first holes and the wavelength $\lambda = 330$ nm defined by the maximum in the PSD agree with the predictions by linear theory $t_{\mathrm{rup}} = 23 \times 10^3$s and $\lambda_{\mathrm{max}} = 340$ nm but are systematically larger than the experimental measurements $t_{\mathrm{exp}} = (2.8 \pm 0.5) \times 10^3$ s and $\lambda_{\mathrm{exp}} = (166 \pm 47)$ nm, Supplementary Note 9.

However, the power spectral densities of the initially prepared interfaces, Fig. 3a, b reveal that the initial roughness of the experimentally prepared interfaces is not composed of white noise but rather of colored noise with a tendency for larger amplitudes at longer wavelengths. Moreover, the initial roughness of the PS-PMMA and the PS-air interface is positively correlated for wavelengths at the micrometer scale. To mimic the experimentally observed colored noise, we introduce the following model for initial data

$$h(t=0,\boldsymbol{x}) = h^0 + \sum_{\boldsymbol{k}} \frac{\delta h^0}{|\boldsymbol{k}|^\rho}\, \xi(\boldsymbol{k}) \cos(k_x x) \cos(k_y y),$$
$$h_\alpha(t=0,\boldsymbol{x}) = h^0_\alpha + \sum_{\boldsymbol{k}} \frac{\delta h^0_\alpha}{|\boldsymbol{k}|^\rho}\, \xi_\alpha(\boldsymbol{k}) \cos(k_x x) \cos(k_y y),$$

for $\alpha =$ PMMA with $\boldsymbol{k} = (k_x, k_y) \in \frac{\pi}{L}(m_x, m_y)$ for $m_x, m_y = 1, \ldots, N$ and N being the pixel resolution of the AFM scan or the resolution of the computational mesh used for the solution of (3). By $\xi_\alpha(\boldsymbol{k})$ we denote normally distributed random variables with variance one and δh^0, $\delta h^0_{\mathrm{PMMA}}$ chosen so that the variance of h and h_{PMMA} matches the experimental observations. A comparison of generated and experimental noise in the Supplementary Note 4 shows that colored noise with $\rho = 1$ describes the initial experimental data of the PS-PMMA interface very well. In particular descibes the colored noise the experimental situation much better than white noise with $\rho = 0$. The observation of colored noise is explained theoretically by the assumption of equipartition of energy in fluctuating interfaces[60].

Motivated by the previous observation that noise on interfaces is correlated, we consider the case where $\xi_\alpha(\boldsymbol{k}) = \xi(\boldsymbol{k})$, i.e., that the roughness of the PS-air and PS-PMMA interface are positively or negatively correlated for each $\boldsymbol{k}$ depending on the signs δh_α. In accordance to the linear stability analysis and the associated eigenvalue problem shown in Fig. 5, we choose initial data on the stable and unstable branch via

$$\text{stable: } \delta h^0 = 1.2\,\text{nm}, \quad \delta h^0_{\mathrm{PMMA}} = 1.2\,\text{nm},$$
$$\text{unstable: } \delta h^0 = 0, \quad \delta h^0_{\mathrm{PMMA}} = 1.2\,\text{nm},$$

where $\delta h^0 = \delta h^0_{\mathrm{PMMA}} + \delta h^0_{\mathrm{PS}}$, which is a sufficiently good approximation to the stable and unstable eigenvector for sufficiently large k. The values of $\delta h^0, \delta h$ are chosen to roughly match the observed variations in the experimental data. The topography of such a generated noisy interface is shown in the Supplementary Note 4 together with the log-PSD.

The resulting nonlinear simulations with colored noise and initial data on the stable and unstable branch of the dispersion relation are shown in Fig. 6, while Fig. 7 depicts the corresponding power spectral densities. For stable initial perturbations, all $\boldsymbol{k}$-components fade out quickly except for a small remainder. These remaining components overlap with unstable eigenmodes and are amplified considerably later in the dynamics. This finally leads to rupture at $t_{\mathrm{sim,s}} = 30 \times 10^3$ s, which is slightly longer compared to the linear stability with $t_{\mathrm{rup}} = 23 \times 10^3$ s. Due to the decay of the initial roughness at early times, the evolution falls back into the linear regime and remains there for a considerable part of the evolution. Hence, for stable initial perturbations, the fastest-growing mode can fully develop and become clearly visible in the PSD and the normalized PSD in Fig. 7a, c. This fastest-growing wavelength

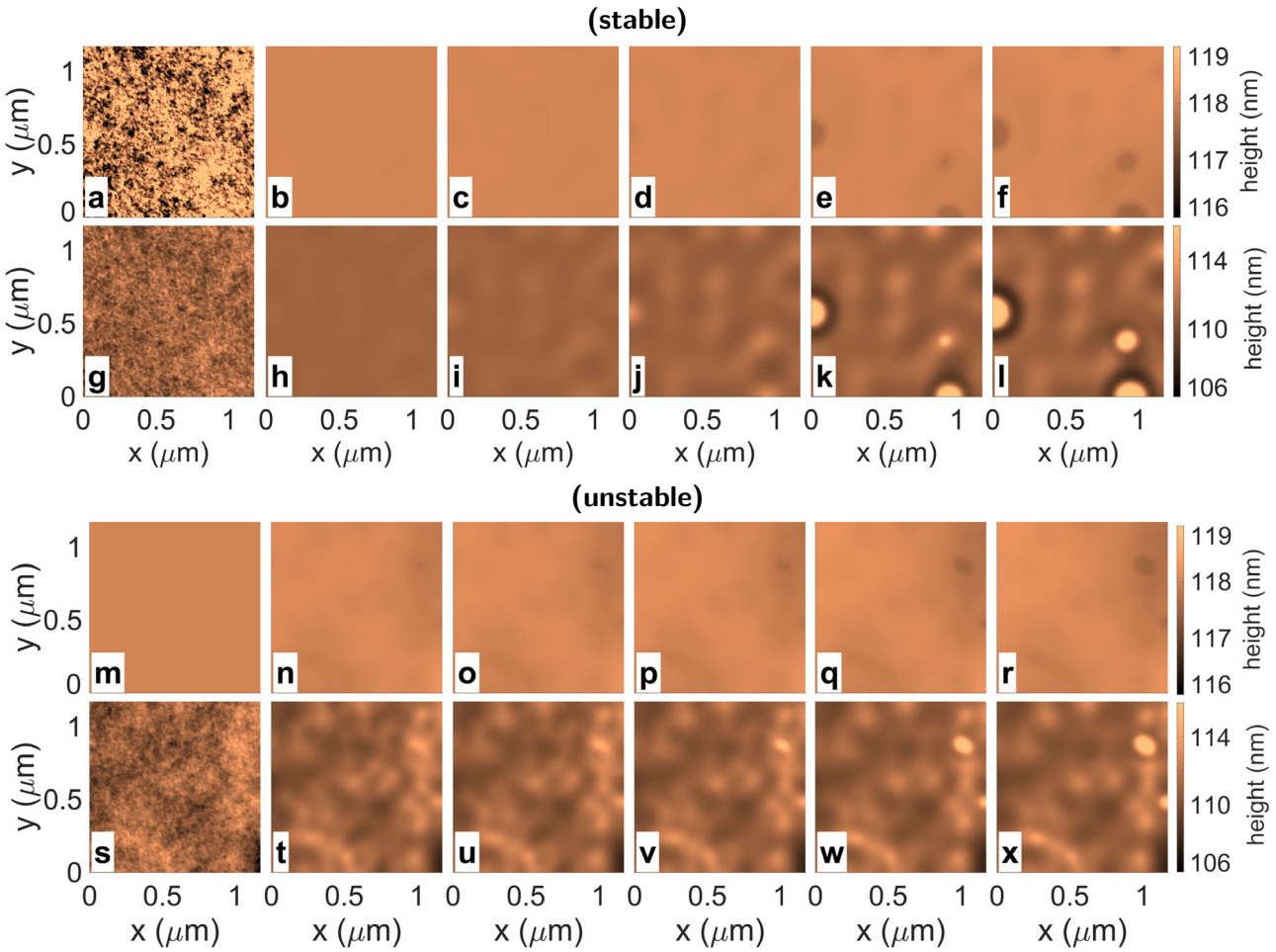

Fig. 6 Numerical solutions of the evolution of polystyrenen(PS)-air and PS-polymethylmethacrylate (PMMA) interfaces for different initial perturbations. As start configuration the interfaces are perturbed by colored noise, Supplementary Note 4, **a**–**l** on the stable and **m**–**x** on the unstable branch. Images **a**–**f** and **m**–**r** show the PS-air surfaces, $h(t,\boldsymbol{x}) = h_{\mathrm{PMMA}}(t,\boldsymbol{x}) + h_{\mathrm{PS}}(t,\boldsymbol{x})$ and images **g**–**l** and **s**–**x** show the corresponding PS-PMMA interfaces, $h_{\mathrm{PMMA}}(t,\boldsymbol{x})$. The film thicknesses for both, stable and unstable initial data, are $h^0_{\mathrm{PS}} = 7$ nm and $h^0_{\mathrm{PMMA}} = 111$ nm. The panels of initial stable corrugations **a**–**l** denote $t = \{0, 9.8, 19.6, 26.9, 30.3, 31.3\} \times 10^3$ s; appearance of first holes at $t \sim 30 \times 10^3$ s. Time steps of the initial unstable corrugations **m**–**x** denote $t = \{0, 0.39, 0.59, 0.81, 1.22, 1.47\} \times 10^3$ s; appearance of first holes at $t \sim 0.8 \times 10^3$ s. Times increase from left to right. Later stages of the evolution are shown in Supplementary Note 10.

$\lambda_{\mathrm{sim,s}} = (350 \pm 80)$ nm is again compatible with $\lambda_{\mathrm{max}} = 340$ nm from linear theory.

For unstable initial perturbations, nonlinear effects lead to a strong acceleration of the rupture for all wavelength with $\lambda \geq \lambda_{\mathrm{crit}}$ compared to the linear theory. To this end, we specifically point out the comparison of linear and full nonlinear theory with colored noisy initial perturbations in the Supplementary Note 4, where we verify the nonlinear acceleration of spinodal rupture quantitatively for stable and unstable perturbations. The initially larger amplitude of larger wavelength results in the power spectral density shown in Fig. 7b with no local maximum identifiable at any time, similar to the experimental PSD of the PS-air interface in Fig. 3a. The unstable wavelength predicted from linear theory cannot be identified here because the initial data started already in the nonlinear regime and unstable perturbations have not enough time to grow out of the initial spectrum. Notably, if the PSD is normalized with respect to the initial spectrum at $t = 0$, the resulting maximum in the PSD in Fig. 7d gives a striking local maximum at a much lower maximum wavelength $\lambda_{\mathrm{sim,u}} = (210 \pm 50)$ nm. This value is in fact well below the unstable wavelength $\lambda_{\mathrm{max}} = 340$ nm predicted by the linear theory for this PS film thickness, and even slightly below the predicted critical wavelength $\lambda_{\mathrm{crit}} = 230$ nm that is the limit for positive amplification in the linear stability theory. The immediate amplification for unstable initial perturbations also leads to a much smaller theoretical rupture time of $t_{\mathrm{sim,u}} = 0.8 \times 10^3$ s for unstable initial perturbations, which is about $30\times$ faster than prediction from linear stability $t_{\mathrm{rup}} = 23 \times 10^3$ s and more than three times faster than the corresponding experimental rupture time $t_{\mathrm{exp}} = (2.8 \pm 0.5) \times 10^3$ s for $h^0_{\mathrm{PS}} = 7$ nm, Fig. 4b. The fact that wavelengths below λ_{crit} are amplified also emphasizes the need of a nonlinear analysis.

In the specific numerical example with unstable initial roughness, both the spinodal wavelength and the breakup time are closer to the experimental data than predicted by the preceding linear stability analysis. The main difficulty in the predicting power is the assumed decomposition of the initial data into stable and unstable components. While the relevance of colored noise for this prediction is evident, the experiment only provides clear evidence for correlation of the noise for longer wavelengths around 1 μm and not in the relevant region of the spinodal wavelength near λ_{max}. A possible unstable (antiphase) correlation of the initial conditions at wavelength around λ_{max} cannot be established because of the very small spinodal wavelength of about 150 nm for the example of $h_{\mathrm{PS}} = 7$ nm and the limited experimental accuracy.

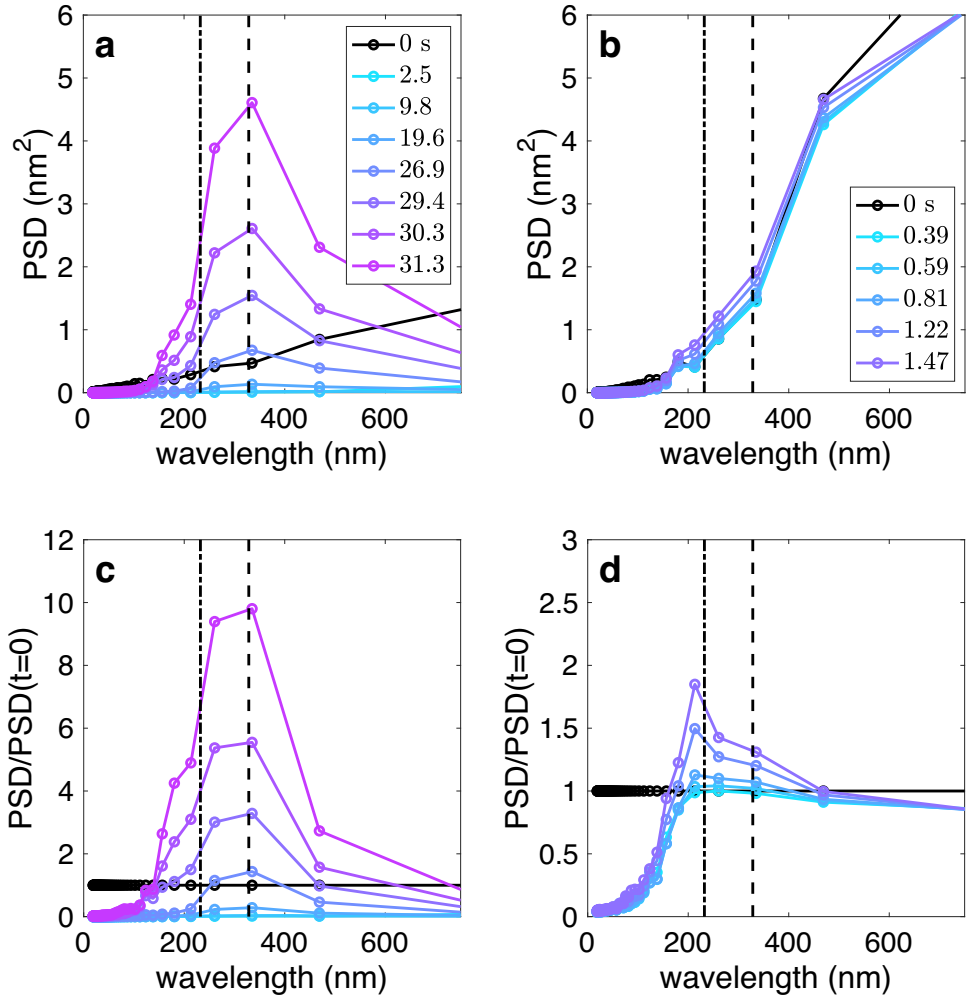

Fig. 7 Power spectral densities (PSD) of numerically generated polystyrene (PS)-polymethylmethacrylate (PMMA) interfaces with different initial perturbations. Power spectral density of h_{PMMA} at different times t for the numerical solutions of Fig. 6 shown for stable perturbation **a** and for unstable perturbations **b**. Corresponding PSDs normalized with respect to the PSD at $t = 0$ are shown in **c** for stable perturbation and in **d** for unstable perturbations. The dashed line in each panel shows the fastest-growing wavelength λ_{max} and the dash-dotted line shows the critical wavelength λ_{crit} from the linear stability analysis. The times in the legends of **a**, **b** are given in units of 10^3 s.

While we mainly investigated the effects of nonlinear amplification of colored noise, thermal fluctuations are expected to contribute significantly to the dynamics if the fluctuations are excited in the unstable region of the dispersion relation.

Conclusion

AFM-based experimental observations of spinodal dewetting of a thin liquid polystyrene (PS) film from a liquid polymethylmethacrylate (PMMA) layer were compared with theoretical predictions. While the experimentally observed trends of preferred wavelength and rupture time for variable PS thickness and the negative correlation of PS-air and PS-PMMA interfaces match expectations from linear stability analysis, the experimental values for spinodal wavelength and rupture time are still systematically smaller than predictions from linear theory. Even if all experimental uncertainties in physical parameters such as the Hamaker constant, short-range part of the effective interface potential, polymer viscosities, possible interfacial slip, and measurement errors taken together may account for this difference, it seems very unlikely that all errors point in the same direction, in particular, as their values are well established in literature.

In contrast to spinodal dewetting from a solid support[17,19,20], where the dispersion relation features one branch only and thermal noise speeds-up the dewetting[26–28], we find that for liquid–liquid dewetting both the mode selection process and the rupture time depend sensitively on initial roughness of both interfaces. This dependence on initial roughness arises from the existence of two solution branches, one stable and one unstable, where for unstable modes the dynamics with realistic colored noise easily falls into the nonlinear region and therefore deviates significantly from linear theory. A direct comparison of linear vs nonlinear rupture for random perturbations on the stable and unstable branch of the dispersion relation is provided in the Supplementary Note 5. The impact of roughness on the model selection process that was observed in this study can also clarify previously reported discrepancies between experimentally derived and calculated Hamaker constant and in particular can answer the sensitivity on the preparation protocol observed[40].

Applying uncorrelated white noise as start configuration for both interfaces, the nonlinear simulations reproduced expectations from linear stability analysis. Starting with colored noise at both interfaces and correlating the noise of both interfaces to be on the stable branch does not impact the selected spinodal wavelength, but rather prolongs the breakup time as the stable modes first reduce before the unstable modes grow again. However, starting with colored noise on the unstable branch strongly

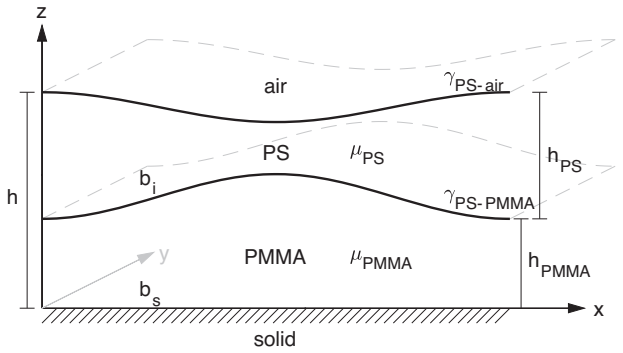

Fig. 8 Geometric setup of bilayer system. The system is characterized by the total height h and the individual heights or viscosities of polystyrene (PS) and polymethylmethacrylate (PMMA) layers h_{PS} and h_{PMMA} or μ_{PS} and μ_{PMMA}, respectively. The PS/PMMA interface has the interfacial tension $\gamma_{PS\text{-}PMMA}$ and the PS-air surface has the surface tension $\gamma_{PS\text{-}air}$. The solid-PMMA interface the slip length b_s and the PMMA-PS interface the slip length b_i.

reduces the wavelength of the fastest-growing modes and shortens the breakup time and thus significantly impacts the mode selection process. In this context, we have also shown that the roughness modes that are relevant for mode selection and that need to be correlated are around the spinodal wavelength.

Since the amplification of the modes on the unstable branch starts immediately and the system begins with finite amplitudes of the wavelengths around the spinodal wavelength (predicted by the linear stability), the respective starting configuration dominates in the power spectral density analysis. When focusing on the amplification of modes, wavelengths below the spinodal wavelength dominate and their maximum was found to be even in the range of the critical wavelength. Moreover, for the example of $h_{PS} = 7$ nm, the resulting rupture time on the unstable branch is significantly reduced to a fraction 1/30 of the original value compared to the expectations from the linear stability analysis.

We conclude that the inclusion of spatial roughness and spatio-temporal fluctuations of both interfaces is crucial in the quantitative description of spinodal dewetting of liquid bilayer systems. Besides the demonstrated importance of initial roughness of both interfaces that might result from a certain preparation process or the molecular nature of the used liquids, it seems similarly important considering spatio-temporal thermal noise that is also expected to behave differently at the liquid-air and the buried liquid-liquid interface. Our results thus call for an extension of the current theory for liquid–liquid dewetting and the inclusion of thermal fluctuations that will theoretically further underpin our results and establish new patterns of liquid–liquid systems, such as found in Supplementary Note 12. This will require the derivation of a fully stochastic thin film model for liquid–liquid systems, for which currently no theoretical work exists but whose need has been demonstrated here.

Methods

Thin-film model and linear stability. Spinodal dewetting of a liquid polystyrene film (PS) on top of a liquid polymethylmethacrylate substrate (PMMA) is considered as shown in Fig. 8.

We assume the flow to be governed by the incompressible Navier-Stokes equation, where the free capillary boundary is driven by an intermolecular potential $\Phi(h)$ that destabilizes the PS layer and leads to spinodal dewetting[44]. The common long-wave approximation then provides the evolution equation of the simplified system

$$\partial_t \boldsymbol{h} = \nabla \cdot \left[\boldsymbol{Q}(\boldsymbol{h}) \nabla \frac{\delta \mathcal{E}}{\delta \boldsymbol{h}} \right], \tag{3}$$

where $\boldsymbol{h}(t,\boldsymbol{x}) = (h_{PMMA}(t,\boldsymbol{x}), h_{PS}(t,\boldsymbol{x}))$ with the total nondimensional height $h = h_{PS} + h_{PMMA}$, the degenerate mobility matrix $\boldsymbol{Q} = \boldsymbol{Q}_{visc} + \boldsymbol{Q}_{slip}$, and where

$$\mathcal{E}(\boldsymbol{h}) = \int_\Omega \frac{\gamma}{2} |\nabla h_{PMMA}|^2 + \frac{1}{2} |\nabla h|^2 + \Phi(h_{PS})\, \mathrm{d}\boldsymbol{x}. \tag{4}$$

is the energy functional with the nondimensional surface-tension ratio $\gamma = \gamma_{PS\text{-}PMMA}/\gamma_{PS\text{-}air}$. Details are given in Supplementary Note 1, including the numerical approach for solving the nonlinear evolution problem (3).

Sample preparation and AFM measurements. Polystyrene (PS) films with a molecular weight of 63 kg mol^{-1} and thicknesses in the range of ($2\,\mathrm{nm} \le h_{PS}^0 \le 10\,\mathrm{nm}$) were prepared on top of polymethylmethacrylate (PMMA) with molecular weight of 10 kg mol^{-1} and a thickness of either $h_{PMMA}^0 = (111 \pm 4)$ nm or $h_{PMMA}^0 = (219 \pm 7)$ nm. The molecular weights of the polymers were chosen as short as possible to consider them as Newtonian liquids and as long as needed to allow for the preparation of the thin film while guaranteeing a viscosity ratio of PS and PMMA of about one. The PMMA films were spin-coated from toluene solution onto cleaned silicon wafer cuts. Cleaning of the silicon wafer was done by a fast CO_2 stream (Snow-Jet, Tectra), sonication in ethanol, acetone and toluene, followed by Piranha etch[61]. The rms roughness of the polished and cleaned silicon wafers was determined by AFM on an areas of 1 μm^2 and were reliably less than 0.2 nm. PS layer were prepared by spin coating from toluene solution on freshly cleaved Mica sheets and subsequently transferred onto the PMMA coated silicon cuts. Transferring was achieved by floating the PS layer onto ultrapure water (GenPure UV/UF, Fisher Scientific) and picking up with the PMMA coated silicon wafer from above; film thicknesses were determined by ellipsometry (EP3, Accurion).

The glass transition temperature of PS(63k) is $T_{G,PS} = (95\pm5)$ °C, while that of PMMA(10k) is $T_{G,PMMA} = (115\pm5)$ °C[36]. Both polymers were purchased from Polymer Standard Service Mainz (PSS-Mainz, Germany) with polydispersities of $M_w/M_n = 1.03$ for the PS and of $M_w/M_n = 1.05$ for the PMMA. The surface tension of the PMMA-air interface is assumed as $\gamma_{PMMA\text{-}air} = (32 \pm 2)$ mN m^{-1}, that of the air-PS interface is $\gamma_{PS\text{-}air} = (31.5 \pm 0.2)$ mN m^{-1}, i.e., about 25 times larger than that of the buried PS-PMMA interface $\gamma_{PS\text{-}PMMA} = (1.25 \pm 0.07)$ mN m^{-1} [36,62].

The dewetting processes were monitored in situ by atomic force microscopy in soft tapping mode (AFM, Bruker, Dimension Icon, fast scan) at temperatures in the range of (120−130) °C to adapt the dynamics of the system to the imaging speed of the AFM. As no change of T_G or polymer viscosity is expected for nanometric PS layers on PMMA substrates thicker than 35 nm[63–65], we assume bulk values for the polymer viscosities, which agree with viscosity measurement in thin films[36] using the leveling method[66,67] that have recently been extended to bilayer systems[68]. The viscosity of PS in this temperature range varies between 0.98 MPas $\lesssim \mu_{PS} \lesssim$ 9.8 MPas and between 0.71 MPas $\lesssim \mu_{PMMA} \lesssim$ 6.5 MPas of PMMA[69]. The resulting viscosity ratio of PS and PMMA is thus $\mu = 1.5$ for $T = 120$ °C and $\mu = 1.38$ for $T = 130$°C. A potential impact of remaining solvents or residual stresses in solvent cast polymer films on the dewetting process, as was observed for large molecular weight polymer films dewetting from slippery surfaces with large contact angle[70,71], was tested using different protocols: Ready prepared samples were stored at room temperature for 2 months before conducing the dewetting experiments; spin coated PMMA films on silicon wafers were preannealed either for 2 h at 55 °C or for 45 min at 145 °C, while spin coated PS films on mica surfaces were preannealed either for 2 h at 55 °C or for about 5 min at 115 °C before transferring them at room temperature on the preannealed PMMA surfaces and to finalize the sample used for the dewetting experiments. However, no influence of aging or preannealing was detected on the dewetting process, so that the influence of residual stresses can be safely excluded for the present results. Since no influence of the drying or preaging protocols were observed, these additional steps were not conducted routinely.

To reveal the 3D shape of both the PS-air and that of the buried PS-PMMA interface, dewetting scenarios were imaged ex situ. For that, samples were quenched from dewetting temperatures down to room temperature at a desired dewetting stage and the frozen dewetting pattern was imaged by AFM with great accuracy. Subsequently, the PS layer was removed by dipping the glassy polymer sample in a selective solvent (cyclohexane, Sigma Aldrich, Germany) for 5 s at 50 °C and immediately blow-dried with a gentle stream of nitrogen gas. The formerly buried PS-PMMA interfaces could then be imaged by AFM and be aligned with that of the PS-air interface to obtain full three-dimensional images.

A slightly different protocol was used to obtain the initial topography data of the PMMA interface shown in Figs. 1 and 2a, f for $t = 0$. In this cases, the PMMA interfaces were scanned after spin coating at room temperature to obtain the topography of the PMMA interface and the same spot was scanned again after transferring the PS layer onto the underlying PMMA layer to obtain the topography of the PS-air interface. We validated this procedure and with it the protocol of PS film removal, by comparing the thus obtained topographies of the PMMA interface with topographies that were obtained following our typical procedure, i.e. scanning the PMMA interface after preparation of the complete PMMA-PS sample and subsequently removing the PS layer with a selective solvent, i.e. as done for all subsequent dewetting situations for times $t > 0$. The obtained PMMA topography was independent on the applied protocol.

Assuming a single electronic absorption frequency of 3×10^{15} Hz[51, p. 186] and relative permittivities of air, PS, and PMMA as $\varepsilon_r = \{1.00059, 2.6, 2.6\}$ and the corresponding refractive indices as $n_r = \{1.00029, 1.5894, 1.4893\}$[72], respectively, the Hamaker constant for the two-interface system air-PS-PMMA was calculated

using the formalism in[51]

$$A = 1.49 \times 10^{-20}\mathrm{J}. \quad (5)$$

Despite a realistic uncertainty in the order of $\pm 0.4 \times 10^{-20}$ J, the positive Hamaker constant A implies that a PS film on top of PMMA is spinodally unstable, leading to spinodal film breakup of sufficiently thin films. The free energy (4) of the air/PS/PMMA/Si system can be modeled as[21]

$$\Phi(h) = -\frac{A}{12\pi h_{\mathrm{PS}}^2} - \frac{A_1}{12\pi h_{\mathrm{PMMA}}^2} - \frac{A_2}{12\pi h^2} + \frac{B}{h_{\mathrm{PS}}^n}. \quad (6)$$

where, in addition to the Van der Waals forces encoded by the Hamaker constants, stabilizing intermolecular forces are encoded in B and n. From[21] we get $A_1 = 3.81 \cdot 10^{-20}$ J and $A_2 = -23.02 \cdot 10^{-20}$ J, which are negligible due to $(h_{\mathrm{PS}}/h_{\mathrm{PMMA}})^2 \sim 10^{-2}$ and we set $A_1 = A_2 = 0$ for simplicity. Commonly used values for n are $3 \le n \le 8$[73], where we are using $n = 4$. $(h_{\mathrm{PS}}/h_{\mathrm{PMMA}})^2 \sim 10^{-2}$. We refer to our Supplementary Note 2 for further details regarding the effective interface potential.

Data availability

Experimental raw data, and the ascii data of the experimental data shown in the figures are available at Zenodo: https://doi.org/10.5281/zenodo.6475157.

Code availability

Simulation codes, and the ascii data of the simulation data shown in the figures and the matlab codes to generate them are available at Zenodo: https://doi.org/10.5281/zenodo.6475157.

Received: 25 August 2022; Accepted: 17 April 2023;
Published online: 22 May 2023

References

1. De Gennes, P.-G. Wetting: statics and dynamics. *Rev. Modern Phys.* **57**, 827 (1985).
2. Bonn, D., Eggers, J., Indekeu, J., Meunier, J. & Rolley, E. Wetting and spreading. *Rev. Modern Phys.* **81**, 739 (2009).
3. Snoeijer, J. H. & Andreotti, B. Moving contact lines: scales, regimes, and dynamical transitions. *Annual Rev. Fluid Mech.* **45**, 269–292 (2013).
4. Wyart, F. B., Martin, P. & Redon, C. Liquid/liquid dewetting. *Langmuir* **9**, 3682–3690 (1993).
5. Lal, J. et al. Universal dynamics of coarsening during polymer-polymer thin-film spinodal dewetting kinetics. *Phys. Rev. E* **102**, 032802 (2020).
6. Huh, C. & Scriven, L. E. Hydrodynamic model of steady movement of a solid/liquid/fluid contact line. *J. Colloid Interf. Sci.* **35**, 85–101 (1971).
7. Cox, R. The dynamics of the spreading of liquids on a solid surface. part 1. viscous flow. *J. Fluid Mech.* **168**, 169–194 (1986).
8. Voinov, O. Hydrodynamics of wetting. *Fluid Dyn.* **11**, 714–721 (1976).
9. Blake, T. & Haynes, J. Kinetics of liquidliquid displacement. *J. Colloid Interf. Sci.* **30**, 421–423 (1969).
10. Hardy, W. B. Iii. the spreading of fluids on glass. *London, Edinburgh, Dublin Philosoph. Mag. J. Sci.* **38**, 49–55 (1919).
11. Cahn, J. W. Critical point wetting. *J. Chem. Phys.* **66**, 3667–3672 (1977).
12. Shikhmurzaev, Y. D. Moving contact lines in liquid/liquid/solid systems. *J. Fluid Mech.* **334**, 211–249 (1997).
13. Jacqmin, D. Contact-line dynamics of a diffuse fluid interface. *J. Fluid Mech.* **402**, 57–88 (2000).
14. Craster, R. V. & Matar, O. K. Dynamics and stability of thin liquid films. *Rev. Modern Phys.* **81**, 1131 (2009).
15. Mukherjee, R. & Sharma, A. Instability, self-organization and pattern formation in thin soft films. *Soft Matter* **11**, 8717–8740 (2015).
16. Reiter, G. Dewetting of thin polymer films. *Phys. Rev. Lett.* **68**, 75 (1992).
17. Seemann, R., Herminghaus, S. & Jacobs, K. Dewetting patterns and molecular forces: a reconciliation. *Phys. Rev. Lett.* **86**, 5534 (2001).
18. Xie, R., Karim, A., Douglas, J. F., Han, C. C. & Weiss, R. A. Spinodal dewetting of thin polymer films. *Phys. Rev. Lett.* **81**, 1251 (1998).
19. Seemann, R., Herminghaus, S. & Jacobs, K. Gaining control of pattern formation of dewetting liquid films. *J. Phys.: Condensed Matter* **13**, 4925 (2001).
20. Becker, J. et al. Complex dewetting scenarios captured by thin-film models. *Nat. Mater.* **2**, 59–63 (2003).
21. Pototsky, A., Bestehorn, M., Merkt, D. & Thiele, U. Alternative pathways of dewetting for a thin liquid two-layer film. *Phys. Rev. E* **70**, 025201 (2004).
22. Bandyopadhyay, D., Gulabani, R. & Sharma, A. Instability and dynamics of thin liquid bilayers. *Ind. Eng. Chem. Res.* **44**, 1259–1272 (2005).
23. Fisher, L. & Golovin, A. Nonlinear stability analysis of a two-layer thin liquid film: Dewetting and autophobic behavior. *J. Colloid Interf. Sci.* **291**, 515–528 (2005).
24. Neto, C. et al. Satellite hole formation during dewetting: experiment and simulation. *J. Phys.: Condensed Matter* **15**, 3355 (2003).
25. Peschka, D. et al. Signatures of slip in dewetting polymer films. *Proc. Nat. Acad. Sci.* **116**, 9275–9284 (2019).
26. Davidovitch, B., Moro, E. & Stone, H. A. Spreading of viscous fluid drops on a solid substrate assisted by thermal fluctuations. *Phys. Rev. Lett.* **95**, 244505 (2005).
27. Grün, G., Mecke, K. & Rauscher, M. Thin-film flow influenced by thermal noise. *J. Stat. Phys.* **122**, 1261–1291 (2006).
28. Fetzer, R., Rauscher, M., Seemann, R., Jacobs, K. & Mecke, K. Thermal noise influences fluid flow in thin films during spinodal dewetting. *Phys. Rev. Lett.* **99**, 114503 (2007).
29. De Gennes, P.-G., Brochard-Wyart, F. & Quéré, D. *Capillarity and Wetting Phenomena: Drops, Bubbles, Pearls, Waves* (Springer Science & Business Media, 2013).
30. Lambooy, P., Phelan, K. C., Haugg, O. & Krausch, G. Dewetting at the liquid-liquid interface. *Phys. Rev. Lett.* **76**, 1110–1113 (1996).
31. Qu, S. et al. Dewetting dynamics at a polymer- polymer interface. *Macromolecules* **30**, 3640–3645 (1997).
32. Segalman, R. A. & Green, P. F. Dynamics of rims and the onset of spinodal dewetting at liquid/liquid interfaces. *Macromolecules* **32**, 801–807 (1999).
33. Geoghegan, M. & Krausch, G. Wetting at polymer surfaces and interfaces. *Progr. Polymer Sci.* **28**, 261–302 (2003).
34. Yadavali, S., Krishna, H. & Kalyanaraman, R. Morphology transitions in bilayer spinodal dewetting systems. *Phys. Rev. B* **85**, 235446 (2012).
35. Bommer, S. et al. Droplets on liquids and their journey into equilibrium. *Eur. Phys. J. E* **36**, 87 (2013).
36. Peschka, D., Bommer, S., Jachalski, S., Seemann, R. & Wagner, B. Impact of energy dissipation on interface shapes and on rates for dewetting from liquid substrates. *Sci. Rep.* **8**, 1–11 (2018).
37. Sferrazza, M. et al. Evidence for capillary waves at immiscible polymer/polymer interfaces. *Phys. Rev. Lett.* **78**, 3693 (1997).
38. Sferrazza, M. et al. Interfacial instability driven by dispersive forces: The early stages of spinodal dewetting of a thin polymer film on a polymer substrate. *Phys. Rev. Lett.* **81**, 5173–5176 (1998).
39. Higgins, A. et al. The timescale of spinodal dewetting at a polymer/polymer interface. *Eur. Phys. J. E* **8**, 137–143 (2002).
40. de Silva, J. P. et al. Switching layer stability in a polymer bilayer by thickness variation. *Phys. Rev. Lett.* **98**, 267802 (2007).
41. Pototsky, A., Bestehorn, M., Merkt, D. & Thiele, U. Morphology changes in the evolution of liquid two-layer films. *J. Chem. Phys.* **122**, 224711 (2005).
42. Pototsky, A., Bestehorn, M., Merkt, D. & Thiele, U. Evolution of interface patterns of three-dimensional two-layer liquid films. *EPL (Europhys. Lett.)* **74**, 665 (2006).
43. Bandyopadhyay, D. & Sharma, A. Nonlinear instabilities and pathways of rupture in thin liquid bilayers. *J. Chem. Phys.* **125**, 054711 (2006).
44. Jachalski, S., Peschka, D., Münch, A. & Wagner, B. Impact of interfacial slip on the stability of liquid two-layer polymer films. *J. Eng. Math.* **86**, 9–29 (2014).
45. Danov, K. D., Paunov, V. N., Alleborn, N., Raszillier, H. & Durst, F. Stability of evaporating two-layered liquid film in the presence of surfactant-i. the equations of lubrication approximation. *Chem. Eng. Scie.* **53**, 2809–2822 (1998).
46. Karapetsas, G., Craster, R. V. & Matar, O. K. Surfactant-driven dynamics of liquid lenses. *Phys. Fluids* **23**, 122106 (2011).
47. Huth, R., Jachalski, S., Kitavtsev, G. & Peschka, D. Gradient flow perspective on thin-film bilayer flows. *J. Eng. Math.* **94**, 43–61 (2015).
48. Amarandei, G. et al. Pattern formation induced by an electric field in a polymer–air–polymer thin film system. *Soft Matter* **8**, 6333–6349 (2012).
49. Thiele, U., Velarde, M. G. & Neuffer, K. Dewetting: Film rupture by nucleation in the spinodal regime. *Phys. Rev. Lett.* **87**, 016104 (2001).
50. Verma, R. & Sharma, A. Defect sensitivity in instability and dewetting of thin liquid films: Two regimes of spinodal dewetting. *Ind. Eng. Chem. Res.* **46**, 3108–3118 (2007).
51. Israelachvili, J. N. *Intermolecular and surface forces* (Academic press, 2011).
52. Vaynblat, D., Lister, J. R. & Witelski, T. P. Rupture of thin viscous films by van der waals forces: Evolution and self-similarity. *Phys. Fluids* **13**, 1130–1140 (2001).
53. Ward, M. H. Interfacial thin films rupture and self-similarity. *Phys. Fluids* **23**, 062105 (2011).
54. Mecke, K. & Rauscher, M. On thermal fluctuations in thin film flow. *J. Phys.: Condensed Matter* **17**, S3515 (2005).
55. Nesic, S., Cuerno, R., Moro, E. & Kondic, L. Fully nonlinear dynamics of stochastic thin-film dewetting. *Phys. Rev. E* **92**, 061002 (2015).

56. Hirai, Y., Yoshikawa, T., Takagi, N., Yoshida, S. & Yamamoto, K. Mechanical properties of poly-methyl methacrylate (pmma) for nano imprint lithography. *J. Photopolymer Sci. Technol.* **16**, 615–620 (2003).
57. Fernandez, M. et al. Neutron reflection investigation of the interface between an immiscible polymer pair. *Polymer* **29**, 1923–1928 (1988).
58. Schubert, D. & Stamm, M. Influence of chain length on the interface width of an incompatible polymer blend. *EPL (Europhys. Lett.)* **35**, 419 (1996).
59. Sferrazza, M., Bucknall, D. G., Xiao, C. & Jones, R. A. L. Interface width of low-molecular-weight immiscible polymers. *J. Phys.: Condens. Matter* **13**, 10269 (2001).
60. Henle, M. L. & Levine, A. J. Capillary wave dynamics on supported viscoelastic films: single and double layers. *Phys. Rev. E* **75**, 021604 (2007).
61. Lessel, M. et al. Self-assembled silane monolayers: an efficient step-by-step recipe for high-quality, low energy surfaces. *Surface Interf. Anal.* **47**, 557–564 (2015).
62. Wu, S. Surface and interfacial tensions of polymer melts. ii. poly (methyl methacrylate), poly (n-butyl methacrylate), and polystyrene. *J. Phys. Chem.* **74**, 632–638 (1970).
63. Roth, C. B., McNerny, K. L., Jager, W. F. & Torkelson, J. M. Eliminating the enhanced mobility at the free surface of polystyrene: fluorescence studies of the glass transition temperature in thin bilayer films of immiscible polymers. *Macromolecules* **40**, 2568–2574 (2007).
64. Yoon, H. & McKenna, G. B. Substrate effects on glass transition and free surface viscoelasticity of ultrathin polystyrene films. *Macromolecules* **47**, 8808–8818 (2014).
65. Hsu, D. D., Xia, W., Song, J. & Keten, S. Dynamics of interacting interphases in polymer bilayer thin films. *MRS Commun.* **7**, 832–839 (2017).
66. McGraw, J. D., Salez, T., Bäumchen, O., Raphaël, E. & Dalnoki-Veress, K. Self-similarity and energy dissipation in stepped polymer films. *Phys. Rev. Lett.* **109**, 128303 (2012).
67. Salez, T. et al. Numerical solutions of thin-film equations for polymer flows. *Eur. Phys. J. E* **35**, 1–9 (2012).
68. Bertin, V., Lee, C. L., Salez, T., Raphaël, E. & Dalnoki-Veress, K. Capillary levelling of immiscible bilayer films. *J. Fluid Mech.* **911**, A13 (2021).
69. Zulli, F., Giordano, M. & Andreozzi, L. Chain-length dependence of relaxation and dynamics in poly (methyl methacrylate) from oligomers to polymers. *Macromolecules* **51**, 1798–1810 (2018).
70. Reiter, G. et al. Residual stresses in thin polymer films cause rupture and dominate early stages of dewetting. *Nat. Mater.* **4**, 754–758 (2005).
71. Kchaou, M. et al. Tuning relaxation dynamics and mechanical properties of polymer films of identical thickness. *Phys. Rev. E* **97**, 032507 (2018).
72. Lide, D. R. *CRC Handbook of Chemistry and Physics: A Ready-reference Book of Chemical and Physical Data* (CRC Press, 1995).
73. Bertozzi, A. L., Grün, G. & Witelski, T. P. Dewetting films: bifurcations and concentrations. *Nonlinearity* **14**, 1569 (2001).

Acknowledgements

The authors acknowledge financial support from the German Research Foundation (DFG) through the projects #167121686 (R. Seemann, B.W.) within the DFG Priority Program SPP 1506 and a follow up program #422786086 (R. Seemann, B.W.) and #422792530 (D.P.) within the DFG Priority Program SPP 2171. D.P. and B.W. thank the Berlin Mathematics Research Center MATH+ and the Einstein Foundation Berlin for support within the Thematic Einstein Semester *Energy-based mathematical methods for reactive multiphase flows* and by project AA2-9. We acknowledge support by the Deutsche Forschungsgemeinschaft (DFG, German Research Foundation) and Saarland University within the 'Open Access Publication Funding' program.

Author contributions

R. Shiri conducted and analyzed experiments, L.S. and D.P. conducted and analyzed numerical results, D.P., B.W. designed and supervised theoretical research, R. Seemann designed and supervised experimental research. All authors discussed the results and wrote the manuscript.

Funding

Open Access funding enabled and organized by Projekt DEAL.

Competing interests

The authors declare no competing interests.

Additional information

Supplementary information The online version contains supplementary material available at https://doi.org/10.1038/s42005-023-01208-x.

Correspondence and requests for materials should be addressed to Dirk Peschka or Ralf Seemann.

Peer review information *Communications Physics* thanks Alireza Mohammad Karim and the other, anonymous, reviewer(s) for their contribution to the peer review of this work. Peer reviewer reports are available.